communications earth & environment

Article

A Nature Portfolio journal

Article in Press

https://doi.org/10.1038/s43247-026-03968-0

Long-term stability of the North Water Polynya and emerging productivity hotspots driven by sea-ice arch dynamics in Nares Strait

Foucaut Tachon[1] ✉, Karen Nieto[1], Philippe Massicotte[1], Philippe Archambault[1], Marie Latil[1], Simon Bélanger[2], Marcel Babin[1], Karl Attard[1,3] & Mathieu Ardyna[1]

Nares Strait, at the southern edge of the Last Ice Area, is a key ecological gateway where seasonal sea-ice arches modulate ice export, stratification and light availability, shaping the timing and intensity of phytoplankton blooms. Using two decades (2003–2023) of satellite sea-ice observations combined with depth-resolved estimates of phytoplankton primary production, we identify two recurrent productivity hotspots with contrasting temporal dynamics. Primary production in the North Water Polynya (*Pikialasorsuaq*/*Sarvarjuaq*) remains remarkably stable over the satellite record, despite pronounced interannual variability in sea-ice conditions. In contrast, a northern hotspot in Kennedy Channel is highly variable and develops only under specific sea-ice arch configurations, with its spatial footprint constrained by underlying local bathymetry. We also observe increasing production in the northern strait, consistent with earlier ice retreat and longer open-water seasons. Together, these results identify sea-ice arches as key physical regulators of ecosystem functioning at the gateway to the Last Ice Area and provide new insights into the stability of the North Water Polynya and its role for regional ecosystems and local communities under ongoing climate-driven environmental changes.

Arctic sea ice is undergoing a rapid decline in both thickness and extent, driven by accelerated polar warming[1,2]. These changes fundamentally alter the balance between light availability and nutrient supply, two key drivers of primary production (PP) in polar marine ecosystems. Thinner and more mobile ice favors earlier under-ice and sea-ice-free phytoplankton blooms[3–5]. Conversely, enhanced stratification resulting from freshwater inputs and surface warming can inhibit vertical nutrient replenishment, ultimately limiting bloom magnitude[6–9]. At a pan-Arctic scale, recent studies report a 30–50% increase in net primary production (NPP) over recent decades, primarily attributed to longer open-water seasons and improved light availability as ice retreats[4,10,11]. However, this global trend masks significant regional contrasts, as PP is also shaped by nutrients inputs from Pacific and Atlantic inflows[9,12], lateral exchanges across shelves, and upwelling along shelf breaks[13–15]. Whether Arctic ecosystems will transition toward higher or lower productivity under continued warming remains an open question and is likely to vary regionally. This uncertainty is particularly pronounced in poorly studied regions, such as the Last Ice Area (LIA) outflow shelf system of the Arctic Ocean, where changes in sea ice cover and sea-ice thickness influence underwater light availability and fluxes of freshwater, but could also modify local biogeochemical conditions through upwellings of nutrient-rich waters[13].

Nares Strait, a narrow (~30 km) channel between Canada's Ellesmere Island and Greenland, is one of the five major gateways through which sea ice is exported from the Arctic Ocean[16] (Fig. 1a). Unlike the broader Fram Strait, ice export through Nares Strait is dominated by multi-year ice (MYI)[17], and is strongly regulated by the seasonal formation of two ice arches in Robeson Channel and Smith Sound[18–20]. These ice arches are large consolidated packs of ice laterally anchored on the coast of narrow passages where the circulation (here southward) stabilizes them. The ice thickness associated with these arches varies between 0.5 and 2 m[20]. These arches can block ice transport for extended periods, effectively shielding the LIA (Fig. 1a), identified as the Arctic region that is expected to lose its perennial ice cover last, from the seasonally ice-free waters of northern Baffin Bay. It has been hypothesized that ice arches act as ecosystem-structuring features,

[1]Laboratoire de Recherche International Takuvik, Québec-Océan, Department of Biology, Université Laval, Sorbonne Université, CNRS, Québec, QC, Canada. [2]Department of Biology, Chemistry and Geography, Québec-Océan, Université du Québec à Rimouski, Rimouski, QC, Canada. [3]Department of Biology, University of Southern Denmark, Odense, Denmark. ✉e-mail: foucaut.tachon@takuvik.ulaval.ca

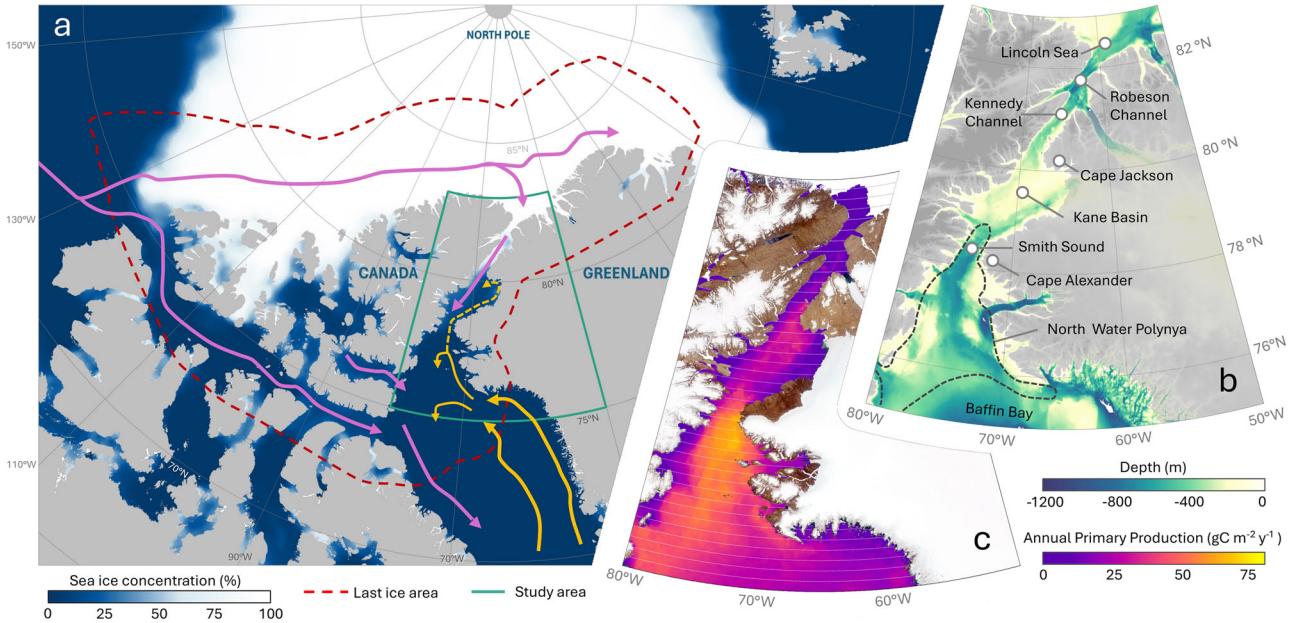

Fig. 1 | General overview of the Nares Strait–Baffin Bay system. a Ice coverage and surface/subsurface circulation in the Canadian Archipelago (yellow arrows for relatively warm water masses and pink arrows for cold water masses). The red dashed polygon represents the Last Ice Area defined by the World Wildlife Fund Canada (WWF). The green polygon represents the study area. Bathymetry of Nares Strait with different locations and the North Water polynya (**b**, black dashed polygon). Annual mean climatology (2003–2023) of primary production across the Nares Strait system, extending from the Lincoln Sea to the North Water Polynya (**c**); with latitudinal bands used for the Hovmöller plots (see Fig. 2).

influencing phytoplankton bloom dynamics at the southern boundary of the LIA by modulating ice export, stratification, and light penetration[21,22]. However, this ecological role has yet to be demonstrated directly, leaving a critical gap in our understanding of how physical processes shape marine productivity in this region.

The North Water Polynya (NOW, *Pikialasorsuaq/Sarvarjuaq*) has long been recognized as one of the most productive polynyas in the Arctic, supporting large phytoplankton blooms and sustaining high biomass[23,24] (Fig. 1). This latent heat polynya is maintained by the release of fusion heat during the ice formation, which is advected with the strong winds and currents[18]. Approximately half of the drifting ice within the polynya is estimated to be thinner than 30 cm[25]. However, recent studies indicate ecological shifts[21,26], including a decline in PP[27,28] and a reduced contribution of diatoms to the phytoplankton community[28]. Several mechanisms have been proposed to explain these trends, including enhanced ice export from Nares Strait, reducing light availability and modifying stratification in the polynya[6,13,29]. Here, we focus specifically on the role of sea-ice dynamics and its influence NPP. These changes have significant implications for regional ecosystems and the ecosystem services they support, from maintaining one of the Arctic's richest food webs to sustaining the cultural and subsistence practices of Inuit communities[30]. These concerns have generated strong interest in better understanding the future trajectory of the NOW, both in terms of Arctic marine ecosystems functioning and the livelihoods of the communities that depend on them.

Contrary to previous observations of decline, our results show that the annual PP in the NOW has remained relatively stable over the past two decades, despite notable changes in ice-arch and sea-ice dynamics. To reconcile this apparent discrepancy, we use two decades (2003–2023) of satellite-derived sea-ice concentration (SIC) data with depth-resolved phytoplankton PP estimates for the whole Nares Strait region. This approach enables us to identify persistent productivity hotspots, assess their contrasting sensitivities to ice-arch dynamics and bathymetric settings, and, to the best of our knowledge, for the first time, demonstrate the role of sea-ice arches as ecosystem structuring features at the southern gateway of the LIA.

Results and discussion

Ice-arch dynamics drives primary production variability

Our analysis of the Nares Strait–Baffin Bay system between 2003 and 2023 highlights a marked spatial heterogeneity in annual PP, spanning more than two orders of magnitude (Fig. 1c). In the Lincoln Sea, values remain below 0.1 gC m^{-2} y^{-1}, whereas recurrently ice-free waters in the NOW sustain rates exceeding 60 gC m^{-2} y^{-1} (Figs. 1 and 2). This variability underscores the tight coupling between PP, open-water area and light availability (Supplementary Fig. 1), but here accentuated by local constraints (Fig. 2). As the sea-ice retreats and the light availability increases, the annual PP is increasing, consistent with pan-Arctic trends[4,11,15] (Fig. 2a). The juxtaposition of perennial ice cover to the north with the highly productive NOW downstream amplifies environmental gradients, locking northern sectors into light-limited regimes while southern regions have been suggested to transition rapidly toward nutrient limitation from a possible increased stratification[7,9,31,32]. Beyond ice dynamics, lateral forcing from outlet glaciers, ice-edge upwellings and the complex bathymetry of Kane Basin and Kennedy Channel further modulate circulation and stratification, shaping nutrient availability and reinforcing sharp contrasts in PP across this outflow shelf system[33–36].

Two recurrent productivity hotspots emerge from the climatological mean map (Fig. 1c) and the Hovmöller diagrams (Fig. 2c). The Southern Hotspot, located near Smith Sound, corresponding to the NOW productive core, sustains the highest mean productivity (51.6 ± 0.2 gC m^{-2} y^{-1}; see Figs. 1 and 3). This persistence suggests favorable local conditions, including recurring thin-ice zones and stratification that reliably trigger under-ice blooms while maintaining sufficient nutrients[15,37]. Consistent with modeling studies of landfast ice-edge upwelling[38] and in situ measurements[39], bloom development is expected to initiate beneath thin ice near the ice edge, after which phytoplankton is mainly advected southward by prevailing currents and then captured by satellites. Contrary to the NOW that has been defined with physical processes[37], we defined it using the remotely sensed primary production (see "Method" in Section 3.2). In contrast, the northern hotspot in Kennedy Channel near Cape Jackson exhibits lower average productivity (27.4 ± 0.2 gC m^{-2} y^{-1}; see Figs. 1–3) but pronounced interannual

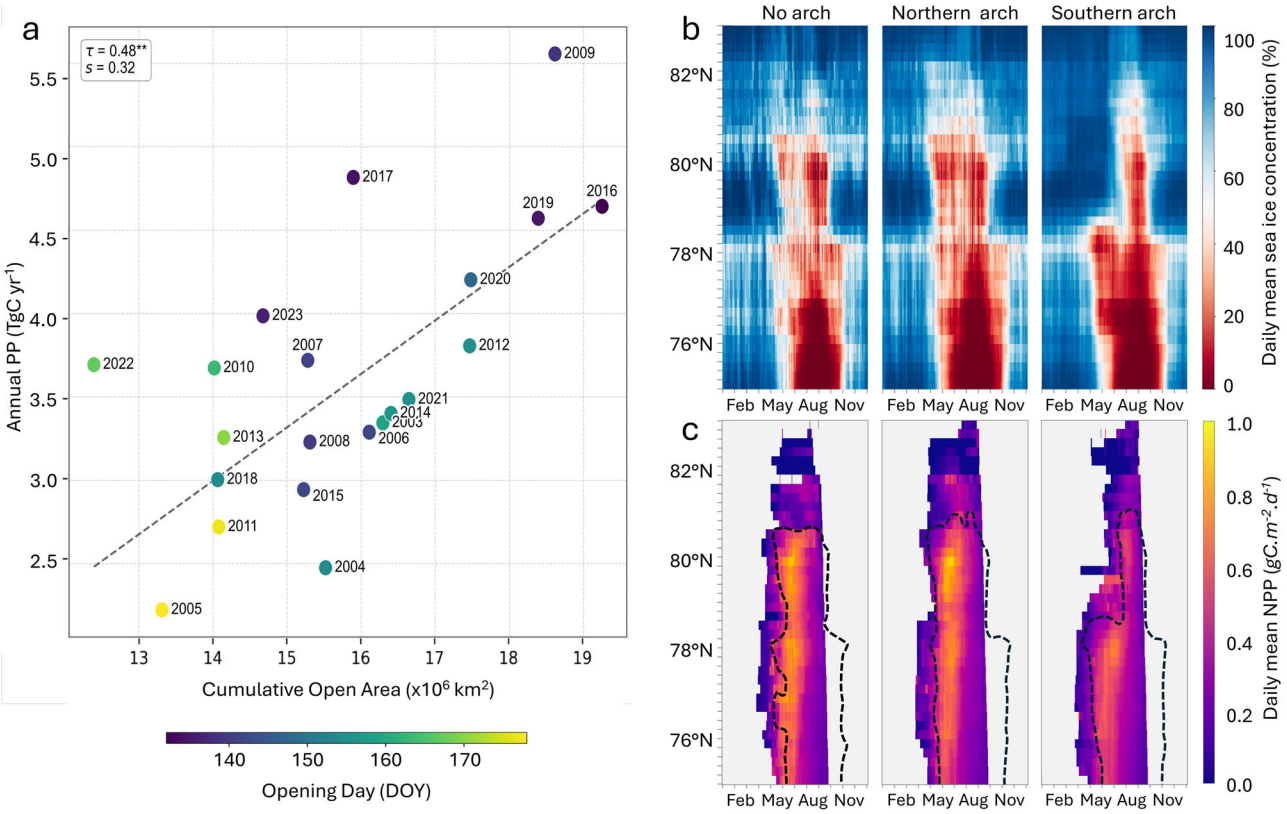

Fig. 2 | Sea-ice concentration and primary production. a Relationship between annual NPP and the open-water area cumulated during the growing season (April–October), with marker color indicating the opening day (OD) when the Nares Strait SIC < 35% for a consecutive 3 weeks. The scatter plot includes a Sen slope (s) with a Kendall rank coefficient (τ), and the asterisks (**) indicate statistically significant correlation ($p < 0.01$). Daily means of sea-ice concentration (**b**, top panel) grouped by arches scenarios and their associated annual primary production associated (respectively, no arches, northern arch, and southern arch scenarios), with a 50% SIC contour (blackline) and net primary production (**b**, bottom panel) along latitude bands (Fig. 1c).

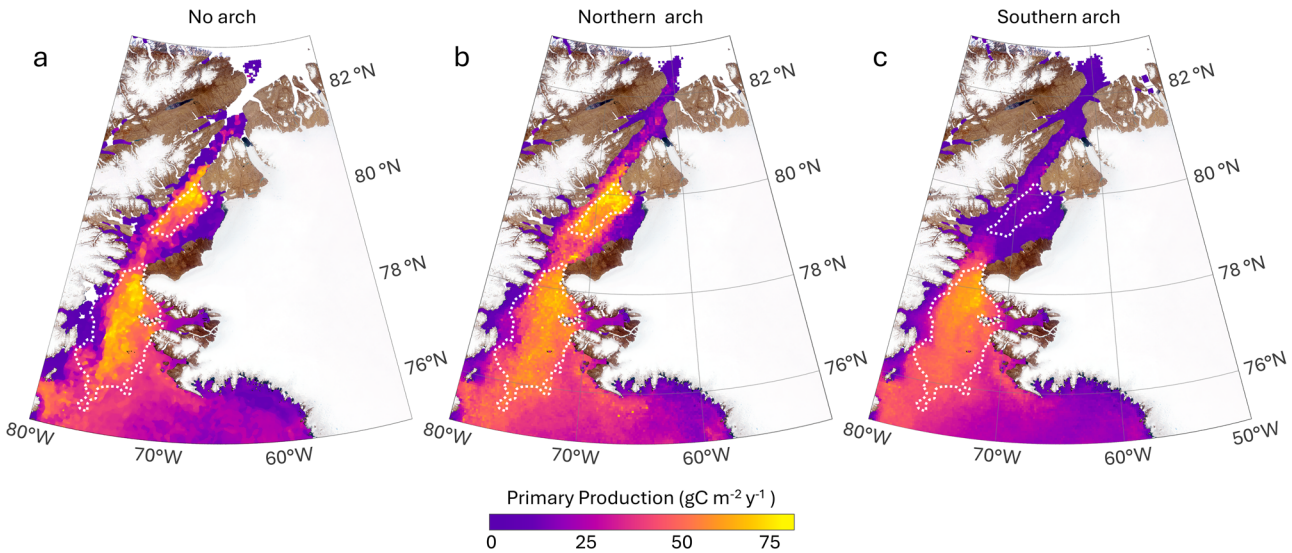

Fig. 3 | Climatological annual PP maps for years with contrasting ice-arch scenarios. a Open years with no ice-arch formation in the Nares Strait–Baffin Bay system (2007, 2022). **b** Years with a persistent northern arch in Robeson Channel (2009, 2010, 2017, and 2019). **c** Closed years with a persistent southern arch in Smith Sound (2003, 2005, 2006, 2008, 2011, 2012, 2013, 2015, 2016, 2018, 2020, 2021, and 2023). White dashed polygons delineate the northern and southern hotspots identified using k-means clustering. Ice-arch scenarios are classified following Moore et al.[20] and Vincent[18].

variability. This northern feature is tightly linked to local conditions of thin ice first described by Kane[40] and more detailed by Kirillov et al.[19,36]. This northernmost sensible heat polynya is explained by the tidal vertical mixing near Cape Jackson, enhanced with the ice-edge upwelling and the cyclonic eddy activity close to the landfast ice edge in the eastern side of Kane Basin, i.e., Peabody Bay[19,35,36,38,40,41]. These conditions collectively generate windows of favorable light and nutrient conditions for bloom development. Together,

Table 1 | Annual PP of the total area, the northern hotspot, and the NOW productive core (in TgC y^{-1}) and their contributions to the total PP (in %)

Year	Northern hotspot (TgC y^{-1})	NOW (TgC y^{-1})	Total (TgC y^{-1})
2003	0.014 (0%)	1.686 (39%)	4.344
2005	0.070 (2%)	1.424 (44%)	3.223
2006	0.057 (1%)	1.781 (42%)	4.289
2007	0.369 (8%)	1.579 (33%)	4.719
2008	0.097 (2%)	1.645 (39%)	4.230
2009	0.443 (7%)	2.025 (31%)	6.557
2010	0.388 (8%)	1.611 (34%)	4.674
2011	0.156 (4%)	1.470 (40%)	3.720
2012	0.060 (1%)	1.862 (39%)	4.806
2013	0.036 (1%)	1.796 (42%)	4.257
2015	0.014 (0%)	1.547 (39%)	3.944
2016	0.111 (2%)	1.886 (33%)	5.643
2017	0.474 (8%)	1.741 (30%)	5.816
2018	0.014 (0%)	1.500 (37%)	4.004
2019	0.425 (8%)	1.445 (26%)	5.571
2020	0.166 (3%)	1.747 (34%)	5.202
2021	0.096 (2%)	1.446 (32%)	4.484
2022	0.349 (7%)	1.615 (34%)	4.693
2023	0.047 (1%)	1.885 (38%)	4.986

these two regions exemplify how the interplay of sea ice, stratification, and bathymetry structures PP at the gateway of the LIA.

Annual PP correlates significantly with the number of open-water pixels during the productive season but not with the timing of break-up, here defined as opening day (April–October; Kendall's $\tau = 0.54$, Mann–Kendall test: $p < 0.001$; Fig. 2a). Yet the absence of a long-term trend in PP (Kendall's $\tau = 0.12$, Mann–Kendall test: $p > 0.05$, see Supplementary Fig. 2) may suggest that productivity trajectories at the LIA gateway are not determined by monotonic sea-ice retreat alone, but by the shifting interplay of ice-arch stability, regional hydrography, bathymetric setting and vertical mixing[19,35,36].

Ice-arch control of productivity hotspots and bloom phenology

While the NOW is characterized by high annual productivity (Table 1 and see Supplementary Fig. 3), finer-scale patterns reveal strong sensitivities to ice-arch dynamics farther upstream in Kane Basin and Kennedy Channel. Clustering analysis (Fig. 3 and see Section 3.4) distinguished two contrasting regions: the NOW productive core, observed consistently across all years with a stable PP, and the northern hotspot, which occurs intermittently depending on ice-arch configuration Table 1.

Ice arches act as mechanical barriers to regulate ice floes entering the strait and the timing of open-water conditions across the system. Consolidation of the northern arch in Robeson Channel suppresses downstream ice flux, leading to prolonged open-water conditions in Kennedy Channel and promoting the development of the northern hotspot, as observed in 2009, 2010, 2017, and 2019 (see Supplementary Fig. 1). Conversely, failure of the southern arch allows open-water conditions extend northward as early as spring, advancing ice breakup in Kane Basin and Kennedy Channel. This favors the initiation of the northern hotspot bloom as early as May, advancing the season by nearly 2 months compared to years when the southern arch persists[18,20]. When both arches failed to consolidate (2007, 2022), ice floes persist across the strait, and the northern hotspot is less productive. These different ice-arches scenarios determine the light availability in Kane Basin and drive the large interannual variability of the northern hotspot.

Beyond affecting the magnitude of NPP, ice-arch dynamics also alter the phenology of northern hotspot blooms[21] by shifting their timing, duration, and seasonal intensity, with potential consequences for food-web coupling and carbon fluxes (Figs. 4 and 5). With a mean of 107 days compared to 44 days (Mann–Whitney U-test: $p = 0.0001$, Fig. 5), the bloom duration of the highest amplitude peak in the northern hotspot significantly extends in the absence of a southern arch. The bloom also occurs at a significantly earlier date with a mean day of the year of 134, in contrast to 202 (Mann–Whitney U-test: $p < 0.001$, Fig. 5) but also with a higher amplitude with a mean of 0.006 TgC d^{-1} compared to 0.002 TgC d^{-1} (Mann–Whitney U-test: $p < 0.001$, Fig. 5). In addition, during open years, a fall bloom can be detected in the northern hotspot further elevating the cumulative annual NPP in the northern hotspot (0.408 TgC y^{-1} compared to 0.072 TgC y^{-1}, Mann–Whitney U-test: $p < 0.001$, Fig. 5). When the northern arch consolidates, annual NPP in the northern hotspot can significantly increase up to 66.6 ± 0.3 gC m^{-2} y^{-1}, nearly six times greater that observed in years with a southern arch (Figs. 3 and 4).

Years of high productivity in the Nares Strait–Baffin Bay system (i.e., 2007, 2009, 2016, 2017, 2019, and 2020) were linked to distinct environmental forcing patterns. For instance, the 2009 season, characterized by a long-lived northern arch and the early collapse of the southern arch, produced anomalously warm conditions[42](+5 °C SST anomaly) and sustained open water that favored prolonged NH blooms. Similarly, 2007 and 2019 were years when the southern arch failed to consolidate entirely, resulting in a more open strait and consequently higher productivity. In contrast, the 2017 season combined thin ice and early collapse with unusual atmospheric forcing linked to the breakdown of the Beaufort High[43] (driven by the anomalously warm autumn of 2016), which left the ice more fractured and led to exceptional bloom conditions in the northern hotspot. Years 2016 and 2020, meanwhile, were associated with a large open-water area extending northwards late in the season, which also supported elevated production.

Stability of the North Water Polynya productivity

By contrast, the productivity of the NOW productive core demonstrates greater stability across all ice-arch scenarios, with an annual mean PP that remains confined within a narrow range despite high SIC variability upstream (Fig. 4). One might expect intensified and earlier northern hotspot blooms to trigger cascading effects downstream, with nutrient depletion and advective transport reducing NPP in the NOW productive core. Yet our results indicate otherwise: NOW productive core PP remains decoupled from the northern hotspot variability. This stability suggests that local upwellings along the eastern side of Greenland described by Dumont et al.[41] dampen the NOW productive core against upstream forcing, decoupling its dynamics from northern variability. Notably, both open water and strong upwelling in this region have long been recognized in Indigenous knowledge systems: *Pikialasorsuaq*, in Kalaallisut, translates as "great upwelling," and *Saravarjuaq* refers to the "place that never freezes" in North Qikiqtaaluk/Baffin Island Inuktitut[44].

This resilience is consistent with the NOW's long-standing recognition as the most productive polynya of the Northern Hemisphere, sustaining intense phytoplankton blooms and supporting one of the richest Arctic food webs[23,37]. Due to its ecological and cultural significance, it has been the focus of numerous studies examining phytoplankton dynamics and ecosystem responses[20,21,26,28,45]. Several of these analyses reported either a decline in net community production (NCP) or PP[26,28], or a reduction in bloom magnitude despite earlier and longer bloom seasons[21]. In this study, we address previous divergent findings using a depth-resolved PP approach applied to an extended 21-year satellite record (2003–2023).

Unlike studies relying solely on surface chlorophyll from satellite ocean color[20,21], our approach integrates depth-resolved PP, explicitly accounting for the subsurface chlorophyll maximum (SCM), which recurrently contributes to total production in Arctic systems[46]. This methodological refinement, in conjunction with an extended time series, partly explains the contrast with earlier findings of decline[21,28]. This discrepancy may reflect a sampling bias, particularly the underestimation of PP occurring deeper in

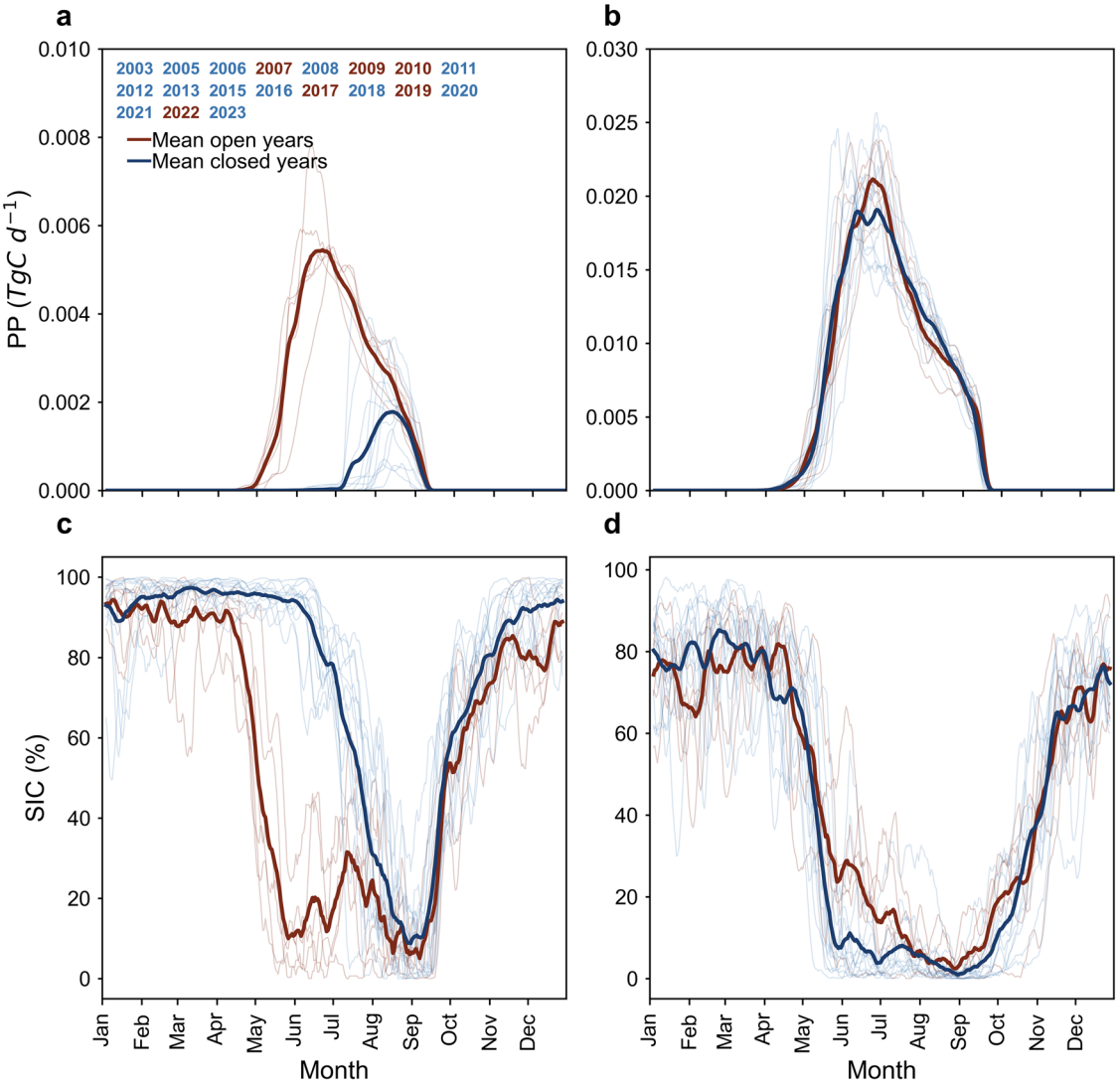

Fig. 4 | Hotspots PP phenology and SIC dynamics. Daily time series of PP (**a**, **b**) and SIC (**c**, **d**) in the northern hotspot (NH) and southern hotspot (SH). Years with a consolidated southern ice arch are shown in blue, and years without are shown in red. Bold lines represent the mean for each scenario.

the water column. Another study by Blais et al.[28] based their conclusions on in situ PP measurements made during CCGS Amundsen expeditions between 2006 and 2011, but their dataset excluded the productive year 2009, when PP reached unusually high values (Fig. 2 and Supplementary Fig. 3). Similarly, Bergeron and Tremblay[26] used a nutrient drawdown time series (1997–2011) that pointed to decreasing NCP. When considering the longer 2003–2023 satellite-derived record, however, annual PP in the NOW shows stability, with a slight positive trend of about +0.18 TgC per decade (see Supplementary Fig. 3). This stability is consistent with recent observations of rising nutrient concentrations in Arctic waters in Nares Strait[47], which may help sustain production despite ongoing sea-ice change.

Our results further confirm the broader stability of the system: PP remains consistently high in the NOW productive core, regardless of ice-arch configuration, with average values of 49.4 ± 0.2, 52.8 ± 0.2, and 51.7 ± 0.2 gC m^{-2} y^{-1} for no-arch, northern-arch, and southern-arch years, respectively (Fig. 3). This is consistent with Moore et al.[20] observations who demonstrated that ice-arch scenarios (southern, northern, or no-arch) exert little influence on ice opening and biomass within the NOW itself. However, their findings were based on surface chlorophyll averages and not on depth-integrated PP. This stability contrasts with the dependence of Kennedy Channel productivity to ice-arch dynamics and highlights the NOW as a resilient system within the LIA.

While the NOW as a whole generally shows stable PP over time (Table 1 and Supplementary Fig. 3), localized spatial heterogeneity exists. An area of recurrent elevated production is observed in its northern sector, near Cape Alexander (Figs. 1 and 2), consistent with local upwelling and cyclonic eddy activity[41]. These mechanisms underpin the system's capacity to sustain high PP across shifting ice regimes, reinforcing the NOW as a critical ecological and cultural stronghold within the Last Ice Area (Table 1 and Supplementary Fig. 3). However, the resilience of the NOW represents only one facet of a more complex arch-dependent productivity regime at the Last Ice Area gateway.

Conclusions

Together, these contrasting hotspots—a transient, arch-dependent northern hotspot and a resilient, locally sustained NOW productive core—demonstrate that sea-ice arches act as ecosystem-structuring features that can regulate the phenology, intensity, and spatial distribution of PP at the southern gateway of the LIA. These dynamics carry direct implications for the functioning and resilience of one of the Arctic's most productive polynyas.

The northern hotspot's dependence on arch consolidation illustrates the sensitivity of high-Arctic regions to shifting ice dynamics, highlighting the vulnerability of this system to accelerating MYI loss and the potential destabilization of these mechanical barriers. Its productivity is strongly

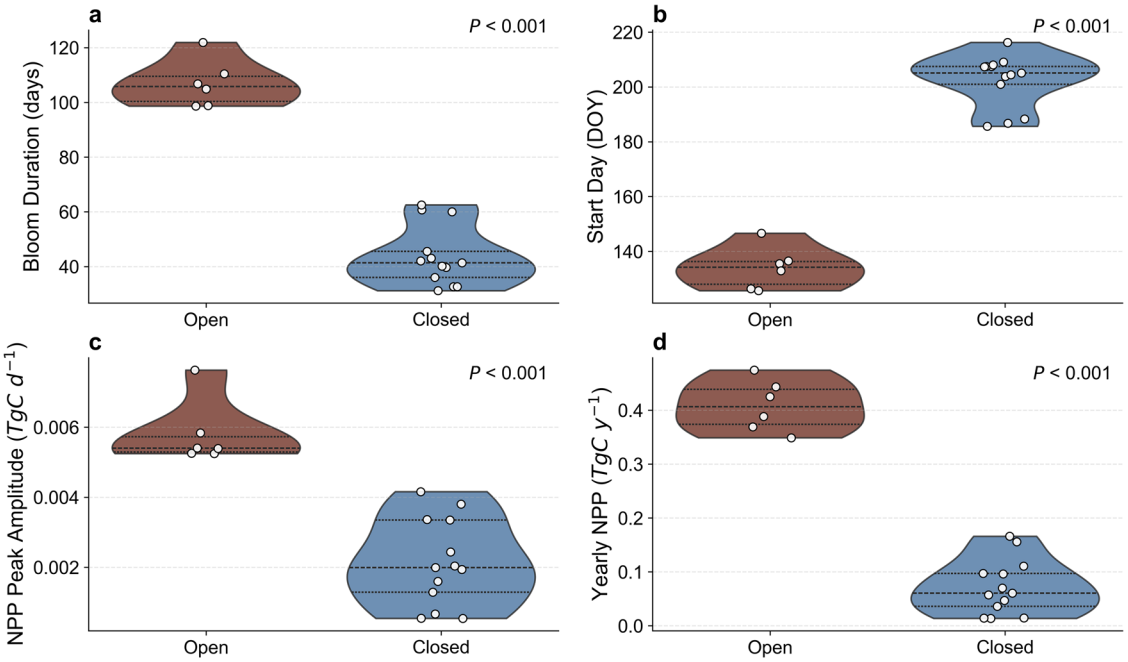

Fig. 5 | Comparative phenological dynamics between open years (blue)— with a southern ice arch—and closed years (red)—without a southern ice arch. Interannual variability and comparison of bloom duration (**a**), start of the season (day of year, **b**), peak NPP amplitude (**c**), and yearly NPP (**d**). Individual raw interannual observations (white markers) are represented with the interquartile range (dotted lines) and the median (dashed line). $n = 6$ (open) and $n = 13$ (closed) independent years. *P*-values were determined by a two-sided Mann–Whitney *U* test.

correlated with the consolidation of the northern arch or the early collapse of the southern arch, both of which determine the duration of the open-water period and, consequently, light availability in Kane Basin. During open years, the northern hotspot bloom occurs earlier (mid-June versus late August; Figs. 4 and 5), with a significantly longer duration and the potential for a secondary autumn bloom (Fig. 4). The NOW, in contrast, sustains similar PP across ice-arch scenarios over two decades of observations, confirming its role as a stable hotspot of productivity within an otherwise variable system.

Taken together, these results demonstrate how sea-ice dynamics influence primary production in an under-explored Arctic outflow. The early phytoplankton blooms enabled by the reduced ice cover, coupled with zooplankton growth, constitute an early food resource for benthic species, fish, mammals, and birds[21,48,49]. These findings support recognizing the NOW as not only a sustained productivity hotspot, but as a keystone ecosystem within the Arctic. The World Conservation Union (IUCN) has already proposed to the United Nation Educational, Scientific and Cultural Organization (UNESCO) to make it a Natural Marine World Heritage Site (WHS) but also the Fisheries and Oceans Canada Department identified it as an Ecologically and Biologically Significant Area (EBSA) due to the importance for Arctic endemic species. Arctic mammals (e.g., Belugas, Narwhals, Polar Bear, Walrus, Seals, and Bowhead Whale), fish (Arctic Cod), and other species rely on the NOW and are important for indigenous communities' way of life[50,51].

Given this ecological and cultural significance, protection of the NOW should be prioritized through marine protected area initiatives and Indigenous stewardship[45,51]. Yet, its future is tied to the broader dynamics of the LIA gateway. As Arctic ice regimes continue to evolve, monitoring the development of the LIA gateway and the NOW in response to unstable ice arches will be important for determining the future of these keystone yet vulnerable ecosystems[30].

Data and methods

Atmospheric and ocean color data

The Santa Barbara DISORT Atmospheric Radiative Transfer model[52] (SBDART) was used, in accordance with Bélanger et al. (2013)[26], to generate look-up tables (courtesy of Simon Bélanger). Subsequently, we use these look-up tables to retrieve the incident spectral downwelling irradiance E_d (0^+, λ, t) at the sea surface (0^+), with a 5 nm spectral resolution (λ) at 3 h timesteps (t). The SBDART model inputs were solar zenith angle (θ_s) and values of cloud fraction (CF) and total ozone concentration (O_3) from MODIS-Aqua (MYD08, https://ladsweb.modaps.eosdis.nasa.gov).

We used the Level-3 binned daily reflectances (Rrs) from the Ocean Colour Climate Change Initiative sinusoidal version 6 product as inputs for the Arctic-optimized version of the semi-analytical Garver–Siegel–Maritorena algorithm (GSM) from Li et al.[53] to generate surface chlorophyll *a* concentration (Chl mg m^{-3}) (OC-CCI v6.0)[54]. Pixels with out-of-range values for the phytoplankton Chl-specific absorption coefficient, spectral decay constant for colored detrital material absorption (aCDM), and power-law exponent for the particulate backscattering spectra from GSM were classified invalid and filtered out following Li et al.[53]. This surface chlorophyll was used to process the different vertical profiles in accordance with Ardyna et al. (2013)[45]. Then the OC-CCI v6.0 Rrs (MERIS bands) were adjusted to generate the PP as in the Bélanger et al. (2013)[26] PP model, based on MODIS spectral bands. This involved shifting the Rrs at 490, 560, and 665 nm to 488, 555, and 667 nm, respectively, without carrying out any operations or modifications, and without any significant impact on the results of the inherent optical properties (IOP)[55]. A linear interpolation between 510 and 560 nm bands were applied to generate Rrs(531). These modified Rrs (488, 531, 555, and 667 nm) were used as inputs for the model.

Sea-ice concentration and ice arches

Daily sea-ice concentration at 12.5 km resolution for the period 2003–2023 was obtained from SSM/I data (CERSAT/Ifremer)[56] using the ARTIST algorithm[57]. Values outside the physical range (0–100%) were removed[58], and a 15% SIC threshold was applied to minimize contamination in ocean-color retrievals near the ice edge[21,59]. Freeze-up and break-up (opening day) were defined according to the adapted Kahru et al.[60] methodology, which defines the open-water period as when the ice fraction is below the threshold of 15% SIC. This method has been adapted with a modified threshold of 35%

SIC and a rolling window of 21 days to filter out short-lived oscillations in ice cover[21,60] (Supplementary Fig. 4).

We classified the years as either open (absence of southern ice arch) or closed (presence of southern ice arch) following the methodology described below. The mean SIC for each latitudinal band from April to June was compared from 2003 to 2023 (Supplementary Fig. 5). Thereafter, a *k*-means clustering method model[61], was employed to categorize each year based on their latitudinal mean SIC gradient (Supplementary Fig. 5). A dendrogram for hierarchical clustering was then applied to ascertain the optimal number of clusters (Supplementary Fig. 5). The present classification is consistent with those reported by Vincent[18] and Moore et al.[20]. However, it should be noted that the present approach highlights only the closed and open years and does not explicitly distinguish no-arch scenarios (Supplementary Fig. 5b). The terminology employed in this paper adopts a different set of ice-arch classification scenarios. Ice-arch configurations are therefore grouped following the framework from Vincent[18] and Moore et al.[20] into three scenarios: a southern arch, when the ice arch is consolidated in Smith Sound; a northern arch, when an ice arch formed in Robeson Channel; and no arch, when neither structure developed during winter. These scenarios capture the primary modes of interannual variability in ice dynamics that modulate sea-ice export through Nares Strait.

TAKUVIK-UQAR primary production model

Primary production was estimated with a depth- and wavelength-resolved model upgraded from Bélanger et al. (2013)[26], as applied in Li et al.[62] and maintained by Takuvik & UQAR (2025)[63]. The upgraded version incorporates improved spatial resolution of atmospheric inputs and a resolution of the vertical Chl a profiles following Ardyna et al. (2013)[45], which captures the typical subsurface chlorophyll maximum found in the Arctic, and of IOP profiles. The carbon fixation rate was calculated daily with the photosynthesis–irradiance model of Platt et al.[64]:

$$PP = P_B^{\max} \int_{t=0}^{24h} \int_{Z_{0.1\%}}^{z_{100\%}} Chl(z)\left(1 - e^{-\frac{PUR(z,t)}{E_k(PUR)}}\right) dz dt,$$

Where Chl(z) is the Chl *a* concentration at depth z (mg m^{-3}), $P_B^{\max}$ is the light-saturated Chl-normalized carbon fixation rate (mgC mgChl^{-1} h^{-1}) set to 2 based on field measurements in Arctic waters[65,66]. $E_k(z)$ is the saturation irradiance modeled here as a function of the spectrally resolved PUR (z, t) (derived from the look-up table in µmol photon m^{-2} s^{-1}). PUR(z), the photosynthetically usable radiation (µmol photon m^{-2} s^{-1}), is estimated as a function of PUR following Huot et al.[66] calculated for each optical depth at a 3 h time interval following Arrigo et al.[67]. The calculated PP, integrated to a maximum depth of 100 m constrained by local bathymetry, was linearly interpolated in time with a maximum 8-day sliding window. Years 2004 and 2014 were excluded due to cloudiness covering more than 50% of the ice-free pixels during both spring and summer (Supplementary Figs. 6 and 7).

Statistical analysis

The *k*-means clustering method[61], which has been previously applied in the Amundsen Sea[68], was applied to the maximum primary production value per pixel subset for the identification of productivity hotspots. This unsupervised classification algorithm partitions pixels into groups based on the similarity of their feature values, here defined as the maximum annual primary production across the time series. Because pixels are assigned according to their distance from mean-based centroids, outliers can strongly influence the clustering. To avoid abrupt pixel-to-pixel variations, we first applied a 7 × 7 median filter to the climatological PP maps to smooth the data and remove outliers before clustering.

We used the Sentinel Application Platform (SNAP)[69] *k*-means cluster analysis algorithm and the number of clusters from 2 to 11. The default parameters for the random seed ($rs = 31415$) and number of iterations ($i = 30$) were used to group pixels with similar production. Based on our observations, we selected $k = 6$ for the clustering, as this configuration clearly highlights the two highly productive areas consistently observed across the time series, with a cluster mean primary production of 47.6 ± 0.2 gC m^{-2} y^{-1}. Using $k = 5$ produces a very similar outcome, while increasing the number of clusters beyond six does not alter the representation of the two productive regions and offers little additional insight. A more exhaustive analysis of the clustering procedure, including sensitivity tests for k, is provided in the Supplementary Information (Supplementary Fig. 8).

The trend analysis over the 21-year time series was performed using the Theil–Sen non-parametric method to remove autocorrelation and outliers from the time series before calculating the trend[26,70]. To assess the significance of the trends, we ran the non-parametric Mann–Kendall test. To compare bloom characteristics—including start, duration, and amplitude—between open and closed arch years, we applied the non-parametric Mann–Whitney *U* test, which does not assume normality and is appropriate for small independent samples. Both the Mann–Kendall and Mann–Whitney *U* test, along with the Theil–Sen slope estimator, were conducted using the *pyMannKendall* and *Scipy* packages from the Python library[71].

Time-frequency bloom detection

To analyze seasonal variability in daily NPP, we used a Python-based time-frequency decomposition using *Scipy.signal* Python library[71] and visually inspected the resulting spectrograms to confirm that the method captured the relevant seasonal scales. A temporally resolved spectrogram was generated (Supplementary Fig. 9) using a Short-Time Fourier Transform (STFT) with a 12-day sliding Hann window (*nperseg*) and 11-day overlap (*noverlap*) to characterize the non-stationary seasonal signal while preserving short-term variability[72]. The high overlap (11/12 = 92%) and 12-day Hann window were chosen to ensure a smooth temporal resolution to be able to capture a 2-week periodicity in NPP. To capture multi-day to seasonal patterns, we removed high-frequency noise by summing the 3 lowest frequencies and applied a 1D median filter to the envelope (*scipy.signal.medfilt*, kernel = 5).

Bloom events were identified from the filtered envelope using the *Scipy* peak detection algorithm based on prominence (*find_peaks*). This algorithm was applied directly on the NPP signal and on the envelope to evaluate the improvements from the STFT approach (Supplementary Fig. 9). Peaks were determined using a minimum temporal spacing of 30 days and a 10% threshold of the annual maximum amplitude to exclude smaller oscillations, although secondary sub-peaks could persist in years with multi-modal structure. The start and end of each bloom were also defined using a relative amplitude criterion, set at 20% of peak height, providing consistent duration estimates even when NPP dampens to zero baseline. For each event, we extracted the day of maximum productivity and the spectral magnitude of the spectrogram if they were quality data. Our approach facilitates the identification of one or more seasonal blooms and their duration, while being insensitive to noise or large data gaps.

To evaluate the added value from our STFT approach, bloom detection results were compared against a simpler baseline method (see Supplementary Fig. 9) in which peaks were identified using the same peak detection criteria but applied on a Gaussian-smoothed NPP signal ($\sigma = 5$ days; *scipy.ndimage.gaussian_filter1d*)[71].

Differences in bloom characteristics between open and closed southern ice-arch scenario conditions were evaluated for three metrics: start day of the bloom with the highest amplitude (day of year), bloom duration, and peak NPP amplitude. We used the non-parametric Mann–Whitney *U* for all comparisons. Data distributions were visualized using a combination of violin plots for the probability density of each metric supplemented with strip plots of the raw data (Fig. 5). The density estimators were constrained ($cut = 0$) to ensure biological plausibility for non-negative metrics. Comparative statistics were conducted at a 95% confidence interval ($\alpha = 0.05$)

Data availability

The original datasets used to reproduce the findings of this study are publicly available on Zenodo for the primary production at https://doi.org/10.5281/

zenodo.20028548. Sea-ice concentration data (12.5 km resolution grids of sea ice concentration from the 85 GHz channel of SSM/I) are available from IFREMER FTP servers at ftp://ftp.ifremer.fr/ifremer/cersat/products/gridded/psi-concentration/data/arctic.

Code availability

The analysis of the model output was done using the open-source software Python. Post-processing scripts will be provided upon request to the corresponding author. The model original code is available on Zenodo at https://doi.org/10.5281/zenodo.14715624.

Received: 10 October 2025; Accepted: 14 August 2026;
Published online: 24 August 2026

References

1. Stroeve, J. & Notz, D. Changing state of Arctic sea ice across all seasons. *Environ. Res. Lett.* **13**, 103001, https://doi.org/10.1088/1748-9326/aade56 (2018).
2. Heuzé, C. & Jahn, A. The first ice-free day in the Arctic Ocean could occur before 2030. *Nat. Commun.* **15**, 1–10, https://doi.org/10.1038/s41467-024-54508-3 (2024).
3. Arrigo, K. R. et al. Phytoplankton blooms beneath the sea ice in the Chukchi Sea. *Deep Sea Res. II* **105**, 1–16, https://doi.org/10.1016/j.dsr2.2014.03.018 (2014).
4. Ardyna, M. & Arrigo, K. R. Phytoplankton dynamics in a changing Arctic Ocean. *Nat. Clim. Change* **10**, 892–903, https://doi.org/10.1038/s41558-020-0905-y (2020).
5. Ardyna, M. et al. Environmental drivers of under-ice phytoplankton bloom dynamics in the Arctic Ocean. *Elem. Sci. Anthr.* **8**, 30, https://doi.org/10.1525/elementa.430 (2020).
6. Tremblay, J. É. & Gagnon, J. The effects of irradiance and nutrient supply on the productivity of Arctic waters: a perspective on climate change. In (eds. Nihoul, J. C. J. & Kostianoy, A. G.) *Influence of Climate Change on the Changing Arctic and Sub-Arctic Conditions*, 73–93. https://doi.org/10.1007/978-1-4020-9460-6 (Springer, 2009).
7. Coupel, P. et al. The impact of freshening on phytoplankton production in the Pacific Arctic Ocean. *Prog. Oceanogr.* **131**, 113125, https://doi.org/10.1016/j.pocean.2014.12.003 (2015).
8. Slagstad, D., Wassmann, P. F. & Ellingsen, I. Physical constraints and productivity in the future Arctic Ocean. *Front. Mar. Sci.* **2**, 85, https://doi.org/10.3389/fmars.2015.00085 (2015).
9. Tremblay, J. É et al. Global and regional drivers of nutrient supply, primary production and CO_2 drawdown in the changing Arctic Ocean. *Prog. Oceanogr.* **139**, 171–196, https://doi.org/10.1016/j.pocean.2015.08.009 (2015).
10. Arrigo, K. R. & van Dijken, G. L. Continued increases in Arctic Ocean primary production. *Prog. Oceanogr.* **136**, 60–70, https://doi.org/10.1016/j.pocean.2015.05.002 (2015).
11. Lewis, K. M., van Dijken, G. L. & Arrigo, K. R. Changes in phytoplankton concentration now drive increased Arctic Ocean primary production. *Science* **369**, 198–202, https://doi.org/10.1126/science.aay8380 (2020).
12. Oziel, L. et al. Environmental factors influencing the seasonal dynamics of spring algal blooms in and beneath sea ice in western Baffin Bay. *Elem. Sci. Anthr.* **7**, 34, https://doi.org/10.1525/elementa.372 (2019).
13. Carmack, E. & Wassmann, P. Food webs and physical–biological coupling on pan-Arctic shelves: unifying concepts and comprehensive perspectives. *Prog. Oceanogr.* **71**, 446–477, https://doi.org/10.1016/j.pocean.2006.10.004 (2006).
14. Michel, C. et al. Arctic Ocean outflow shelves in the changing Arctic: a review and perspectives. *Prog. Oceanogr.* **139**, 66–88, https://doi.org/10.1016/j.pocean.2015.08.007 (2015).
15. Ardyna, M. et al. Shelf-basin gradients shape ecological phytoplankton niches and community composition in the coastal Arctic Ocean (Beaufort Sea). *Limnol. Oceanogr.* **62**, 2113–2132, https://doi.org/10.1002/lno.10554 (2017).
16. Kwok, R. Variability of Nares Strait ice flux. *Geophys. Res. Lett.* **32**, L24502, https://doi.org/10.1029/2005GL024768 (2005).
17. Kwok, R., Pedersen, L. T., Gudmandsen, P. & Pang, S. S. Large sea-ice outflow into the Nares Strait in 2007. *Geophys. Res. Lett.* **37**, L03502, https://doi.org/10.1029/2009GL041872 (2010).
18. Vincent, R. F. A study of the North Water Polynya ice arch using four decades of satellite data. *Sci. Rep.* **9**, 20278. https://doi.org/10.1038/s41598-019-56780-6 (2019).
19. Kirillov, S. et al. On the physical settings of ice bridge formation in Nares Strait. *J. Geophys. Res. Oceans* **126**, e2021JC017331. https://doi.org/10.1029/2021JC017331 (2021).
20. Moore, G. W. K., Howell, S. E. L. & Brady, M. Evolving relationship of Nares Strait ice arches on sea ice along the Strait and the North Water, the Arctic's most productive polynya. *Sci. Rep.* **13**, 9809. https://doi.org/10.1038/s41598-023-36179-0 (2023).
21. Marchese, C. et al. Changes in phytoplankton bloom phenology over the North Water (NOW) Polynya: a response to changing environmental conditions. *Polar Biol.* **40**, 1721–1737, https://doi.org/10.1007/s00300-017-2095-2 (2017).
22. Moore, G. K., Howell, S. E. L., Brady, M., Xu, X. & McNeil, K. Anomalous collapses of Nares Strait ice arches leads to enhanced export of Arctic sea ice. *Nat. Commun.* **12**, 1. https://doi.org/10.1038/s41467-020-20314-w (2021).
23. Tremblay, J. É, Gratton, Y., Fauchot, J. & Price, N. M. Climatic and oceanic forcing of new, net and diatom production in the North Water. *Deep Sea Res. II* **49**, 4927–4946, https://doi.org/10.1016/S0967-0645(02)00171-6 (2002).
24. Bryndum-Buchholz, A., Herbig, J. L., Darnis, G., Geoffroy, M. & Eddy, T. D. Ecosystem structure and function of the North Water Polynya. *Arct. Sci.* **10**, 545568, https://doi.org/10.1139/as-2023-0050 (2024).
25. Schimnowski, O., Paulic, J. E. & Martin, K. A. *Information in Support of the Evaluation of Ecologically and Biologically Significant Areas (EBSA) in the Eastern Arctic Biogeographic Region*. (Fisheries and Oceans Canada, Ecosystems and Oceans Science, 2018).
26. Bergeron, M. & Tremblay, J. É Shifts in biological productivity inferred from nutrient drawdown in the southern Beaufort Sea (2003−2011) and northern Baffin Bay (1997-2011), Canadian Arctic. *Geophys. Res. Lett.* **41**, 3979–3987, https://doi.org/10.1002/2014GL059649 (2014).
27. Bélanger, S., Babin, M. & Tremblay, J. É Increasing cloudiness in the Arctic damps the increase in phytoplankton primary production due to sea-ice receding. *Biogeosciences* **10**, 4087–4101, https://doi.org/10.5194/bg-10-4087-2013 (2013).
28. Blais, M. et al. Contrasting interannual changes in phytoplankton productivity and community structure in the coastal Canadian Arctic Ocean. *Limnol. Oceanogr.* **62**, 2480–2497, https://doi.org/10.1002/lno.10581 (2017).
29. Carmack, E. et al. Climate variability and physical forcing of the food webs and the carbon budget on panarctic shelves. *Prog. Oceanogr.* **71**, 145–181, https://doi.org/10.1016/j.pocean.2006.10.005 (2006).
30. Ribeiro, S. et al. Vulnerability of the North Water ecosystem to climate change. *Nat. Commun.* **12**, 4475. https://doi.org/10.1038/s41467-021-24742-0 (2021).
31. Ardyna, M., Gosselin, M., Michel, C., Poulin, M. & Tremblay, J. É Environmental forcing of phytoplankton community structure and function in the Canadian High Arctic: contrasting oligotrophic and eutrophic regions. *Mar. Ecol. Prog. Ser.* **442**, 37–57, https://doi.org/10.3354/meps (2011).
32. Buchart, L. et al. Future climate scenarios for northern Baffin Bay and the Pikialasorsuaq (North Water Polynya) region. *Atmos. Ocean* **60**, 102–123, https://doi.org/10.1080/07055900.2022.2067028 (2022).
33. Michel, C., Ingram, R. G. & Harris, L. R. Variability in oceanographic and ecological processes in the Canadian Arctic Archipelago. *Prog.*

Oceanogr. **71**, 379–401, https://doi.org/10.1016/j.pocean.2006.09.006 (2006).
34. Münchow, A., Falkner, K. K. & Melling, H. Spatial continuity of measured seawater and tracer fluxes through Nares Strait, a dynamically wide channel bordering the Canadian Archipelago. *Deep Sea Res. I* **54**, 722–742, https://elischolar.library.yale.edu/journal_of_marine_research/183 (2007).
35. Hannah, C. G., Dupont, F. & Dunphy, M. Polynyas and tidal currents in the Canadian Arctic Archipelago. *Arctic* **62**, 83-95, https://doi.org/10.14430/arctic115 (2009).
36. Kirillov, S. et al. The role of oceanic heat flux in reducing thermodynamic ice growth in Nares Strait and promoting earlier collapse of the ice bridge. *Ocean Sci.* **18**, 1535–1557, https://doi.org/10.5194/os-18-1535-2022 (2022).
37. Barber, D. G., Hanesiak, J. M., Chan, W. & Piwowar, J. Sea-ice and meteorological conditions in northern Baffin Bay and the North Water Polynya between 1979 and 1996. *Atmos. Ocean* **39**, 343–359, https://doi.org/10.1080/07055900.2001.9649685 (2001).
38. Clarke, A. J. On wind-driven quasi-geostrophic water movements near fast-ice edges. *Deep Sea Res.* **25**, 41–51, https://doi.org/10.1016/S0146-6291(21)00005-9 (1978).
39. Mundy, C. J. et al. Contribution of under-ice primary production to an ice-edge upwelling phytoplankton bloom in the Canadian Beaufort Sea. *Geophys. Res. Lett.* **36**, 2009GL038837. https://doi.org/10.1029/2009GL038837 (2009).
40. Kane, E. K. *Arctic Explorations: The Second Grinnell Expedition in Search of Sir John Franklin, 1853, '54, '55*, Vol. I, https://doi.org/10.5962/bhl.title (Childs & Peterson, 1856).
41. Dumont, D., Gratton, Y. & Arbetter, T. E. Modeling wind-driven circulation and landfast ice-edge processes during polynya events in northern Baffin Bay. *J. Phys. Oceanogr.* **40**, 1356–1372, https://doi.org/10.1175/2010JPO4292.1 (2010).
42. Vincent, R. F. The 2009 North Water anomaly. *Remote Sens. Lett.* **4**, 1057–1066, https://doi.org/10.1080/2150704X.2013.837227 (2013).
43. Moore, G. W. K., Schweiger, A., Zhang, J. & Steele, M. Collapse of the 2017 winter Beaufort High: a response to thinning sea ice? *Geophys. Res. Lett.* **45**, 2860–2869, https://doi.org/10.1002/2017GL076446 (2018).
44. QIA (Qikiqtani Inuit Association). Sarvarjuaq and Qikiqtait: Inuit Stewardship and the Blue Economy in Nunavut's Qikiqtani Region (Draft). **37**, www.qia.ca. (2020).
45. Olivier, F. et al. Shells of the bivalve *Astarte moerchi* give new evidence of a strong pelagic-benthic coupling's shift occurring since the late 70s in the NOW Polynya. *Philos. Trans. R. Soc. A* **378**, https://doi.org/10.1098/rsta.2019.0353 (2020).
46. Ardyna, M. et al. Parameterization of vertical chlorophyll *a* in the Arctic Ocean: impact of the subsurface chlorophyll maximum on regional, seasonal, and annual primary production estimates. *Biogeosciences* **10**, 4383–4404, https://doi.org/10.5194/bg-10-4383-2013 (2013).
47. Barut, G. et al. Water mass assemblages and nutrient dynamics in Nares Strait: a multiyear perspective. *J. Geophys. Res. Oceans* **130**, e2025JC023074. https://doi.org/10.1029/2025JC023074 (2025).
48. Heide-Jørgensen, M. P. et al. The significance of the North Water Polynya to Arctic top predators. *AMBIO* **42**, 596–610, https://doi.org/10.1007/s13280-012-0357-3 (2013).
49. DFO Identification of Ecological Significance, Knowledge Gaps and Stressors for the North Water and Adjacent Areas. DFO Can. Sci. Advis. Sec. Sci. Advis. Rep. 2021/052 (2021).
50. Flora, J. et al. Present and past dynamics of Inughuit resource spaces. *Ambio* **47**, 244–264, https://doi.org/10.1007/s13280-018-1039-6 (2018).
51. Nuttall, M. *Climate, Capitalism and Communities: An Anthropology of Environmental Overheating* (eds Stensrud, A. B. & Eriksen, T. H.) 57–75 (Pluto Press, 2019).
52. Ricchiazzi, P., Yang, S., Gautier, C. & Sowle, D. SBDART: a research and teaching software tool for plane-parallel radiative transfer in the Earth's atmosphere. *Bull. Am. Meteorol. Soc.* **79**, 2101–2114, https://doi.org/10.1175/1520-0477(1998)079%3c2101:SARATS%3e2.0.CO;2 (1998).
53. Li, J. et al. A tuned ocean color algorithm for the Arctic Ocean: a solution for waters with high CDM content. *Opt. Express* **31**, 38494, https://doi.org/10.1364/OE.500340 (2023).
54. Sathyendranath, S. et al. An ocean-colour time series for use in climate studies: the experience of the Ocean-Colour Climate Change Initiative (OC-CCI). *Sensors* **19**, 4285, https://doi.org/10.3390/s19194285 (2019).
55. Lee, Z., Lubac, B., Werdell, J. & Arnone, R. An update of the quasi-analytical algorithm (QAA_v5). *IOCCG Softw. Rep.* **1**, 1–9 (2009).
56. Ezraty, R., Girard-Ardhuin, F., Piolle, J. F., Kaleschke, L. & Heygster, G. Arctic & Antarctic Sea ice concentration and Arctic sea ice drift estimated from Special Sensor Microwave data—User's manual V2.1. (CERSAT/IFREMER, 2007).
57. Kaleschke, L. et al. SSM/I sea ice remote sensing for mesoscale ocean-atmosphere interaction analysis. *Can. J. Remote Sens.* **27**, 526–537, https://doi.org/10.1080/07038992.2001.10854892 (2001).
58. Andersen, S., Tonboe, R., Kaleschke, L., Heygster, G. & Pedersen, L. T. Intercomparison of passive microwave sea ice concentration retrievals over the high-concentration Arctic sea ice. *J. Geophys. Res. Oceans* **112**, 2006JC003543. https://doi.org/10.1029/2006JC003543 (2007).
59. Bélanger, S., Ehn, J. K. & Babin, M. Impact of sea ice on the retrieval of water-leaving reflectance, chlorophyll a concentration and inherent optical properties from satellite ocean color data. *Remote Sens. Environ.* **111**, 51–68, https://doi.org/10.1016/j.rse.2007.03.013 (2007).
60. Kahru, M., Lee, Z., Mitchell, B. G. & Nevison, C. D. Effects of sea ice cover on satellite-detected primary production in the Arctic Ocean. *Biol. Lett.* **12**, 20160223, https://doi.org/10.1098/rsbl.2016.0223 (2016).
61. Hartigan, J. A. & Wong, M. A. Algorithm AS 136: a K-means clustering algorithm. *Appl. Stat.* **28**, 100, https://doi.org/10.2307/2346830 (1979).
62. Li, J., Matsuoka, A., Pang, X., Massicotte, P. & Babin, M. Performance of algorithms for retrieving chlorophyll a concentrations in the Arctic Ocean: impact on primary production estimates. *Remote Sens.* **16**, 892, https://doi.org/10.3390/rs16050892 (2024).
63. Takuvik & UQAR. *Arctic Ocean Net Primary Production Model Code (v1.0)*. Preprint at https://doi.org/10.5281/zenodo.14715624. (2025).
64. Platt, T. & Gallegos, C. L. Modelling primary production. in (ed. Falkowski, P. G.) *Primary Productivity in the Sea*. Environmental Science Research, Vol 19, https://doi.org/10.1007/978-1-4684-3890-1_19 (Springer, 1980).
65. Harrison, W. G. & Platt, T. Photosynthesis-irradiance relationships in polar and temperate phytoplankton populations. *Polar Biol.* **5**, 153–164, https://doi.org/10.1007/BF00441695 (1986).
66. Huot, Y., Babin, M. & Bruyant, F. Photosynthetic parameters in the Beaufort Sea in relation to the phytoplankton community structure. *Biogeosciences* **10**, 3445–3454, https://doi.org/10.5194/bg-10-3445-2013 (2013).
67. Arrigo, K. R., Worthen, D., Schnell, A. & Lizotte, M. P. Primary production in Southern Ocean waters. *J. Geophys. Res. Oceans* **103**, 15587–15600, https://doi.org/10.1029/98JC00930 (1998).
68. Feng, J., Li, D., Zhang, J., & Zhao, L. Variations and environmental controls of primary productivity in the Amundsen Sea. *Front. Mar. Sci.* **9**, https://doi.org/10.3389/fmars.2022.891663 (2022).
69. SNAP - ESA Sentinel Application Platform v12.0.0, http://step.esa.int.
70. Zhang, X., Vincent, L. A., Hogg, W. D. & Niitsoo, A. Temperature and precipitation trends in Canada during the 20th century. *Atmos. Ocean*

38, 395–429, https://doi.org/10.1080/07055900.2000.9649654 (2000).
71. Virtanen, P. et al. SciPy 1.0: fundamental algorithms for scientific computing in Python. *Nat. Methods* **17**, 261–272, https://doi.org/10.1038/s41592-019-0686-2 (2020).
72. Cohen, L. *Time-Frequency Analysis: Theory and Applications*. (Prentice-Hall, 1995).

Acknowledgements

We sincerely thank the students and researchers who worked at or with the Takuvik lab and put much effort into developing the primary production model. We would like to thank the editor and reviewers for their attention and time during our publication process.

Author contributions

F.T. contributed to the conceptualization, methodology, investigation, visualization, preparation of the original draft, and revision of the manuscript. K.N. contributed to the conceptualization, methodology, interpretation of the results, visualization, and revision of the manuscript. P.M. contributed to the interpretation of results and the revision of the manuscript. P.A. contributed to the supervision of the project, interpretation of results, and the revision of the manuscript. M.L. contributed to the conceptualization. S.B. contributed to the investigation and revision of the manuscript. M.B. contributed to the investigation and revision of the manuscript. K.A. contributed to the supervision of the project, interpretation of results, and the revision of the manuscript. M.A. contributed to the supervision of the project, conceptualization, methodology, interpretation of the results, and revision of the manuscript.

Funding

The primary production model used in this study was developed thanks to support from the Canada Excellence Research Chair on Remote Sensing of Canada's new Arctic Frontier and from the Sentinel North project. The Refuge-Arctic project was conducted using the Canadian research icebreaker CCGS *Amundsen* with the support of the Amundsen Science program funded by the Canada Foundation for Innovation (CFI) Major Science Initiatives (MSI) Fund. The project was conducted under the scientific coordination of the Centre national de la recherche scientifique CNRS/Université Laval Takuvik Joint International Laboratory (IRL3376). We also thank Québec-Océan and the Polar Continental Shelf Program for their in-kind contribution in terms of polar logistics and scientific equipment. The Refuge-Arctic project is funded by the following French and Canadian programs and agencies: Amundsen Science, ArcticNet, BNP Paribas Foundation, Centre National d'études spatiales (CNES) and the CNES-TOSCA "Alg-O-Nord," Centre National de la Recherche Scientifique (CNRS), Crown-Indigenous Relations and Northern Affairs Canada (RCAANC), European Research Council (ERC), Flotte Océanographique française (FOF), Fonds de recherche du Québec - Nature et technologies (FRQNT), Institut Nordique du Québec (INQ), Institut français de recherche pour l'exploitation de la mer (IFREMER), Institut Polaire français Paul-Émile Victor (IPEV), Les Enveloppes Fluides et l'Environnement (LEFE), Mission pour les Initiatives Transverses et Interdisciplinaires (MITI), Natural Sciences and Engineering Research Council of Canada (NSERC), Fisheries and Oceans Canada (DFO), Transforming Climate Action (TCA), Sentinelle Nord and Université Laval. We also wish to thank Denmark's Independent Research Fund (Grant No. 2064-00021B) and the Polar Ocean Mitigation Potential project (Horizon Europe, Grant No. 101136875).

Competing interests

The authors declare no competing interests.

Additional information

Supplementary information The online version contains supplementary material available at https://doi.org/10.1038/s43247-026-03968-0.

Correspondence and requests for materials should be addressed to Foucaut Tachon.

Peer review information *Communications Earth & Environment* thanks Angelika Renner and the other anonymous reviewer(s) for their contribution to the peer review of this work. Primary handling editors: Shenglei Wang and Alice Drinkwater. A peer review file is available.